Materials and Design 144 (2018) 182–191

Contents lists available at ScienceDirect

Materials and Design

journal homepage: www.elsevier.com/locate/matdes

Silicon nanosprings fabricated by glancing angle deposition for ultra-compliant films and interfaces

Dimitrios A. Antartis, Ryan N. Mott, Ioannis Chasiotis *

Aerospace Engineering, University of Illinois at Urbana Champaign, 104 S Wright St, Urbana, IL, USA

HIGHLIGHTS

- Measured the mechanical behavior of Si nanosprings fabricated by Glancing Angle Deposition in tension, compression & bending.
- Obtained the material modulus of aSi nanostructures fabricated by GLAD, ranging from 5 to 50 GPa vs. 94 GPa for bulk aSi.
- The normal and shear stiffness of seeded aSi nanospring films was tuned in the range of 90-1,000 MPa and 15-150 MPa.

GRAPHICAL ABSTRACT

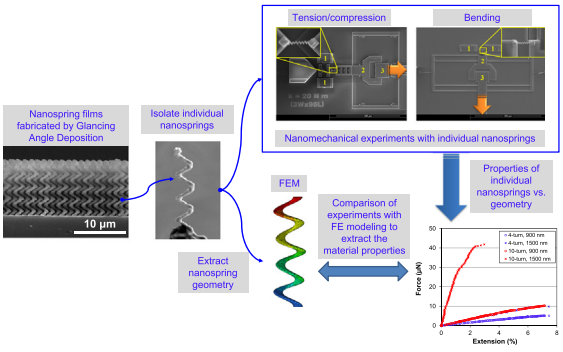

ARTICLE INFO

Article history:
Received 25 October 2017
Received in revised form 5 February 2018
Accepted 5 February 2018
Available online 06 February 2018

Keywords:
Interface toughness
Stress mismatch
Compliance
Microfibrils

ABSTRACT

Micro and nanostructures with well-defined shape and dimensions are the hallmark in the design of scalable nanomaterials, yet the properties and precise geometry of such nanoscale building blocks are largely unknown. This work sheds light into the microstructure, material properties and mechanical behavior of individual nanosprings fabricated by seeded Glancing Angle Deposition (GLAD), with the purpose of designing highly compliant interfaces with drastically reduced coupling between normal and shear deformation. The mechanical response in tension/compression and bending of individual amorphous Si (aSi) nanosprings with 4 or 10 coil turns and different seed spacings was obtained with the aid of MEMS devices: The normal and bending spring stiffness values were in the range of 7–215 N/m and 1–31 N/m, respectively, resulting in estimates for the normal and shear film stiffness in the range of 90–1000 MPa and 15–150 MPa, respectively. The true geometry of GLAD Si springs was determined via SEM tomography and was incorporated in modified analytical and finite element models which, in turn, were used to compute the material modulus of aSi nanostructures fabricated by GLAD. TEM studies revealed that GLAD Si nanosprings are comprised of tightly bundled fine fibrils which impart flaw tolerance and reduce the effective elastic modulus.

1. Introduction

Interfaces are often the weakest link between materials with elastic property mismatch and/or significant differences in the coefficient of thermal expansion. In such material systems, insertion of a compliant interface could mitigate the interfacial stress while increasing the system toughness and resistance to failure. Soft materials, such as polymers and low homologous temperature metals, provide high interfacial compliance, however, at the expense of temperature sensitivity and low strength. Therefore, it becomes apparent that an effective interface material should possess the thermal stability and properties of common

* Corresponding author.
E-mail address: chasioti@illinois.edu (I. Chasiotis).

https://doi.org/10.1016/j.matdes.2018.02.017
0264-1275/

ceramics or metals, and a microstructure that is designed to provide high compliance and resistance to fracture. In the recent years, several applications have been shown to benefit from films comprised of discrete nanoelements, such as thermal interfaces for high power microelectronics [1] and nanostructured thin films for high capacity electrochemical anodes that are subject to large volumetric expansion [2–4]. Films and interfaces comprised of metallic or ceramic nanosprings, for example, reduce the coupling between normal and shear deformation and transform macroscopic shear forces into locally normal and bending forces on individual nanosprings. Such films are often fabricated by Glancing Angle Deposition (GLAD) which does not require photolithography to fabricate intricate, 3D micro and nanostructures. Among the advantages of this method are its compatibility with microelectronics processing, the capability for large area fabrication on virtually any flat surface, and the option to terminate the nanospring arrays with a fully integrated cap that facilitates uniform load transfer to all nanosprings in a film. In general, GLAD can produce films of slanted, straight, or helical micro- or nano-elements of monolithic or hybrid materials [5–10] by controlling the rotation speed of the substrate, the deposition rate, and the deposition angle. By this method, micro or nanostructures grow competitively due to "self-shadowing" because of the very shallow "glancing" angle (>80°) of the incident vapor with respect to the substrate. The nuclei that finally grow form a dense array of slanted columns. If slow substrate rotation is applied, the slanted columns evolve into helices: a full rotation of the substrate results in the growth of one full turn of a helix (spring). Unseeded nanospring films have been the most commonly fabricated GLAD materials, however, according to a recent study [11] they have inconsistent wire thickness and coil diameter, which limit our ability for versatile design of films with desirable mechanical stiffness. On the contrary, substrate seeding yields orderly arrays of nanostructures [12] with uniform geometry and tailorable properties. The latter still remain unexplored, because very little is currently known about the coupled relationships between the GLAD parameters, the material properties of GLAD-deposited structures, and the geometry and mechanical behavior of individual GLAD structures.

This study focuses on the material and mechanical behavior of individual nanosprings in seeded GLAD films comprised of tall Si nanosprings, in order to establish relationships between the deposition parameters and the resulting nanospring geometry and mechanical properties. These fabrication-structure-properties relationships will facilitate the informed design of thin films and interfaces with desirable mechanical behavior that departs from that of bulk metals and ceramics. The few early studies on the mechanics of SiO, Ti, and Cr GLAD films used nanoindentation with a spherical tip and treated the nanospring films as monolithic materials [13,14]. It was assumed that the individual nanosprings are formed by perfectly circular nanowires, which permitted the use of the analytical models by Ancker and Goodier to estimate the spring stiffness [15,16]. However, the shadowing process taking place during GLAD does not imply circular wire cross-sections. Furthermore, the shear response of GLAD spring films, which is of interest in most applications, has only been studied by side-loading the capping layer of Ta_2O_5 nanospring films with an Atomic Force Microscope (AFM) tip [17,18]. Among the shortcomings of these efforts are the application of unaccounted moments by the AFM tip during shear loading, the inability to apply a purely normal force by the tilted AFM cantilever, and the application of a point force on the cap of the film rather than uniform pressure. A direct measurement of the stiffness of individual springs was attempted by Liu et al. [19], who also used an AFM tip to load individual Si springs inside a film. The authors reported spring stiffness values that were lower than expected, attributing the issue to the application of off-axis loading by the AFM tip. However, major uncertainties could also arise from the assumption of a circular wire cross-section to facilitate the use of analytical spring models [15,16] as well as the unknown material properties of GLAD nanostructures.

The present study aims at quantifying and simulating the mechanical behavior of GLAD nanosprings to enable the design of advanced interfaces with desirable normal and shear stiffness. A systematic study of the geometric parameters affecting the mechanical behavior of individual amorphous Si (aSi) nanosprings was carried out. aSi was selected because it is elastic and brittle at room temperature, thus eliminating the convolution of structural spring deformation with material plasticity. Experiments were conducted via Microelectromechanical Systems (MEMS) type devices to measure the mechanical behavior of GLAD nanocolumns and nanosprings in tension, compression and bending. Transmission Electron Microscopy (TEM) and Scanning Electron Microscopy (SEM) studies provided the microstructure and the precise geometry of individual nanosprings. For the first time, an accurate description of the coil and wire geometry was employed in modified analytical models and a Finite Element (FE) model for comparison with the experimental results, which allowed us to estimate the effective material properties of different nanostructures fabricated by GLAD.

2. Experimental methods and materials

2.1. Fabrication of Si nanospring films

Si nanospring films were fabricated by GLAD on unseeded (Fig. 1(a, b)) and seeded (Fig. 1(c–f)) Si substrates at Micralyne in Edmonton, Canada. The seeded films were deposited on a Si wafer in a hexagonal pattern of 500 nm tall Si seed posts with 900 nm or 1500 nm spacing, which were created via Deep Reactive-Ion Etching (DRIE). This seed arrangement generates relatively uniform shadowing during substrate rotation, and thus films with quasi-isotropic in-plane properties. The substrate was titled at 85° and rotated at constant speed to control the wire diameter, coil diameter, and helix angle. The deposition rate was 10 Å/s for all spring types, while the substrate rotation rate was 4.2°/min for 4-turn springs and 10.6°/min for 10-turn springs. The geometry of the resulting structures was spring-like, except for the 10-turn nanosprings with 1500 nm seed spacing that were screw-like (Fig. 1(f)). All nanospring types were 10 ± 0.5 μm high. Similarly, 10 μm long aSi columns were fabricated on seeded substrates to measure the material properties of the GLAD-deposited columns. The unseeded films resulted in highly intertwined springs, with a broad distribution of wire diameters (Fig. 1(a,b)). Therefore, unseeded films provide limited control on the mechanical properties and structural uniformity. The spring intertwining can be reduced by increasing the number of coil turns per unit length, as deduced from a comparison of Fig. 1(a) and Fig. 1(b) where the separation between individual springs was increased by reducing the spring pitch height from 2500 nm (4-turn coils) to 1000 nm (10-turn coils), or by substrate seeding: increased seed spacing reduces the overlap between adjacent springs (Fig. 1(c–f)). Notably, the seed spacing and pitch height not only affect the arrangement of nanosprings but also influence their geometry and properties.

2.2. Mechanical characterization of individual Si nanosprings and nanocolumns

Single nanosprings were isolated under a high magnification optical microscope with a use of a micromanipulation stage, and were placed onto a MEMS device for testing in tension/compression and bending via a MEMS-based optical metrology method [20]. The Si nanosprings were fixed onto the MEMS devices via platinum (Pt) tabs deposited with a Focused Ion Beam (FIB) (Fig. 2(a–d)), which fully constrained the spring ends and approximated fixed-fixed boundary conditions. Ultra-low FIB current averted any deposition of Pt onto the springs. Only springs from seeded substrates (Fig. 1(c–f)) were tested because the density and the irregular geometry of unseeded springs (Fig. 1(a, b)) made it impossible to isolate them from their films. Finally, uniaxial tension experiments with straight Si columns (Fig. 2(e)), also fabricated

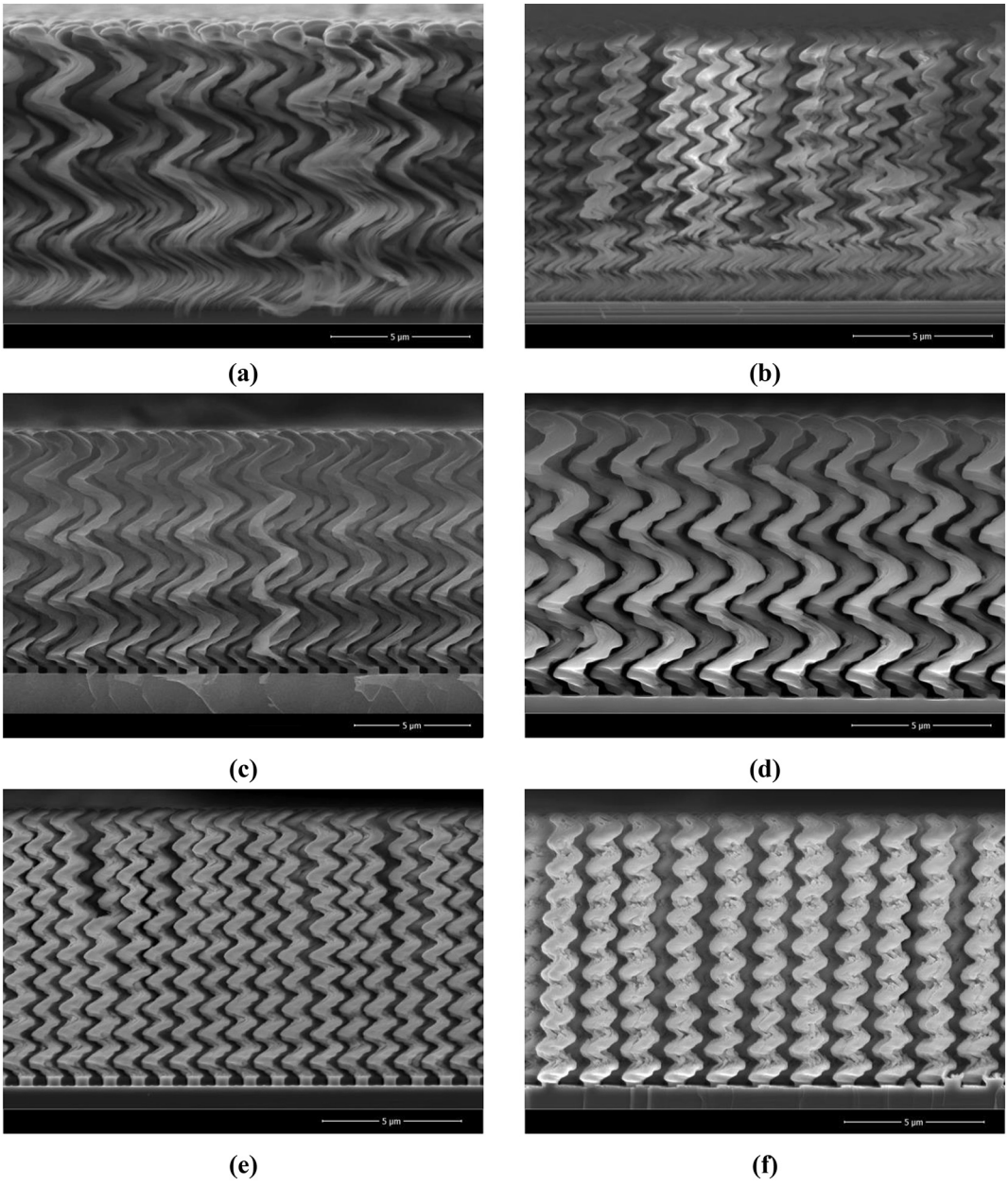

Fig. 1. Side views of uncapped Si nanospring films comprised of (a) 4-turn coils on unseeded substrate, (b) 10-turn coils on unseeded substrate, (c) 4-turn coils with 900 nm seed spacing, (d) 4-turn coils with 1500 nm seed spacing, (e) 10-turn coils with 900 nm seed spacing, and (f) 10-turn coils with 1500 nm seed spacing.

by GLAD on seeded wafers, were performed to measure the unknown elastic modulus of GLAD-deposited aSi at the same conditions as the seeded nanosprings. The 10-μm long Si columns were fabricated with the substrate titled at 85° while rotated at a speed that was at least an order of magnitude faster than the rotation speed for the fabrication of nanospring films [5,6].

Fig. 3(a,b) show the MEMS devices for tension/compression and bending tests, respectively. The applied force is calculated from the opening of the loadcell, namely the relative motion between areas 2 and 3 in Fig. 3(a,b), while, the spring extension/compression or bending is obtained from the crosshead displacement which corresponds to the relative motion between areas 1 and 2. The rigid body displacements of areas 1, 2, and 3 were calculated via Digital Image Correlation (DIC) from dark-field optical images obtained at 400× magnification, with an accuracy of ~0.1 pixels (~20 nm) [20]. The initial tensile (or compressive) nanospring stiffness was measured from the slope of the linear segment of the force vs. nanospring extension (or compression) curves. Similarly, the bending stiffness was calculated from the initial slope of the linear segment of bending force vs. lateral deflection curves. The cross-head loading rate was 30 nm/s and at least three specimens were tested per spring type. The force constant of the MEMS devices was calibrated as described in [21]. MEMS devices with calibrated stiffness of 0.83 N/m and 7.44 N/m were used for the experiments with aSi columns and springs, respectively. These loadcell stiffness values were selected based on the estimated specimen stiffness in order to maximize the measurement accuracy.

2.3. Analytical and numerical modeling of GLAD nanosprings

The experimentally obtained tension/compression stiffness was compared to analytical and numerical modeling predictions. Contrary to prior works, the true, non-circular, geometry of the wires comprising the nanosprings was determined and employed in revised analytical and FE models. Wahl derived the stiffness of a spring with a circular

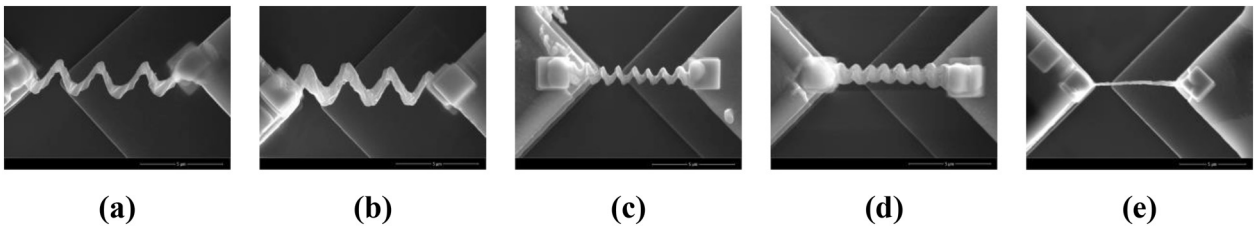

Fig. 2. Si springs isolated from films with (a) 4-turn coils with 900 nm seed spacing, (b) 4-turn coils with 1500 nm seed spacing, (c) 10-turn coils with 900 nm seed spacing, (d) 10-turn coils with 1500 nm seed spacing, and (e) a Si column, mounted onto MEMS devices for testing. All scale bars correspond to 5 μm.

wire cross-section, which is subjected to uniaxial loading while its ends are fixed against rotation as [22,23]:

$$k_a = \frac{Gd^4}{8D^3N}\left(\frac{sin\alpha - sin\alpha_0}{cos^3\alpha_0\left[sin\alpha - sin\alpha_0 + \frac{EI}{GJ}\,tan\alpha(cos\alpha_0 - cos\alpha)\right]}\right)^{-1} \quad (1)$$

where G is the shear modulus, GJ is the torsional rigidity, EI is the flexural rigidity, D is the coil diameter, d is the wire diameter, α is the pitch angle at a given displacement, α_0 is the initial pitch angle, and N is the total number of coil turns. In Wahl's [22,23] and the Ancker and Goodier's model [15,16] described below, the shear modulus G is paired with the polar moment of inertia, I_p, for a circular wire cross-section, which here, for generality, is substituted with the torsional rigidity GJ. Eq. (1) was modified to account for the elliptical wire cross-section of the GLAD springs, which is discussed in the next Section. Then, the axial stiffness of a spring comprised of a wire with an elliptical cross-section and both ends fixed against rotation can be calculated as:

$$k_a = \frac{4GJ}{\pi D^3N}\left(\frac{sin\alpha - sin\alpha_0}{cos^3\alpha_0\left[sin\alpha - sin\alpha_0 + \frac{EI_a}{GJ}\,tan\alpha(cos\alpha_0 - cos\alpha)\right]}\right)^{-1} \quad (2)$$

where the torsional constant of an ellipse with major axis a and minor axis b is given by:

$$J = \frac{\pi a^3 b^3}{\left(a^2 + b^2\right)} \quad (3)$$

and the pitch angle, α, given by [22,23]:

$$tan\alpha = \frac{h_p}{\pi D} \quad (4)$$

where h_p is the pitch length of the spring as shown in Fig. 4(a).

Ancker and Goodier [15,16] derived an equation for the axial stiffness of a spring, assuming radial symmetry (every cross-section of the spring experiences the same load) as:

$$k_a = \frac{Gd^4}{8D^3N}\left[1 - \frac{3d^2}{16D^2} + \frac{1-\nu}{2(1+\nu)}\,tan^2(\alpha)\right]^{-1} \quad (5)$$

Similar to Wahl's model, Eq. (5) was modified here to account for an elliptical cross-section:

$$k_a = \frac{4GJ}{\pi D^3N}\left[1 - \frac{3ab}{4D^2} + \frac{1-\nu}{2(1+\nu)}\,tan^2(\alpha)\right]^{-1} \quad (6)$$

where the d^2 term in Eq. (5) was replaced by $4ab$, as the particular term accounts for the shear deformation in the wire cross-section. The model parameters in Eqs. (2), (6) are shown in Fig. 4(b).

3. Results and discussion

3.1. Geometry of GLAD nanosprings

Detailed SEM imaging (Fig. 5(a)) and FIB-tomography carried out at different angles (Fig. 5(b)) provided the cross-section of the wires forming the seeded nanosprings, which was approximated as elliptical. On the other hand, the coil cross-section is hexagonal (Fig. 5(c)), but could be closely approximated as circular. The hexagonal coil geometry is due to shadowing by the neighboring springs that are arranged in a hexagonal pattern (Fig. 5(d)). This hexagonal arrangement provides the most uniform shadowing during substrate rotation and coil growth, and, thus, quasi-isotropic in-plane properties.

There are several important considerations when evaluating the geometry of GLAD nanosprings. First, it must be noted that uncertainties in the wire dimensions can have significant impact on the nanospring stiffness which scales with the fourth power of the wire diameter, e.g. Eq.

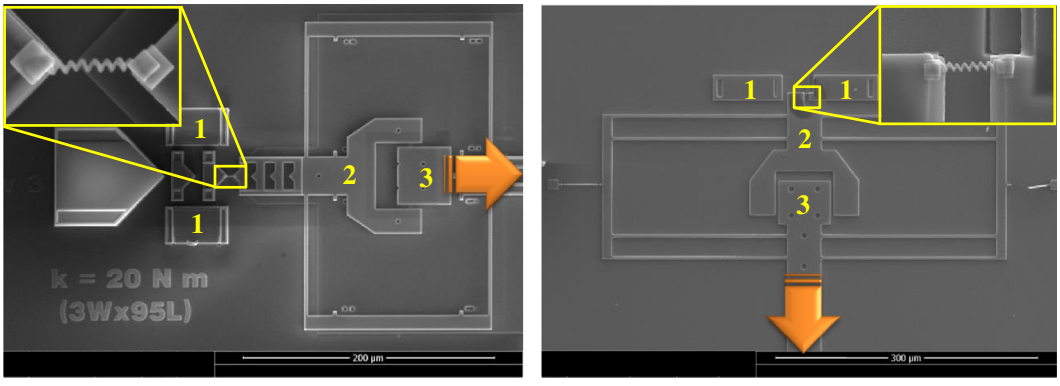

(a) (b)

Fig. 3. (a) A 10-turn spring mounted on a tension/compression MEMS device. (b) A 10-turn spring mounted onto a MEMS device for bending testing. The rigid body displacements of components 1, 2, 3 were computed via DIC. Insets show the 10-turn springs attached to the MEMS device grips with FIB-deposited Pt. The arrows point to the direction of actuation.

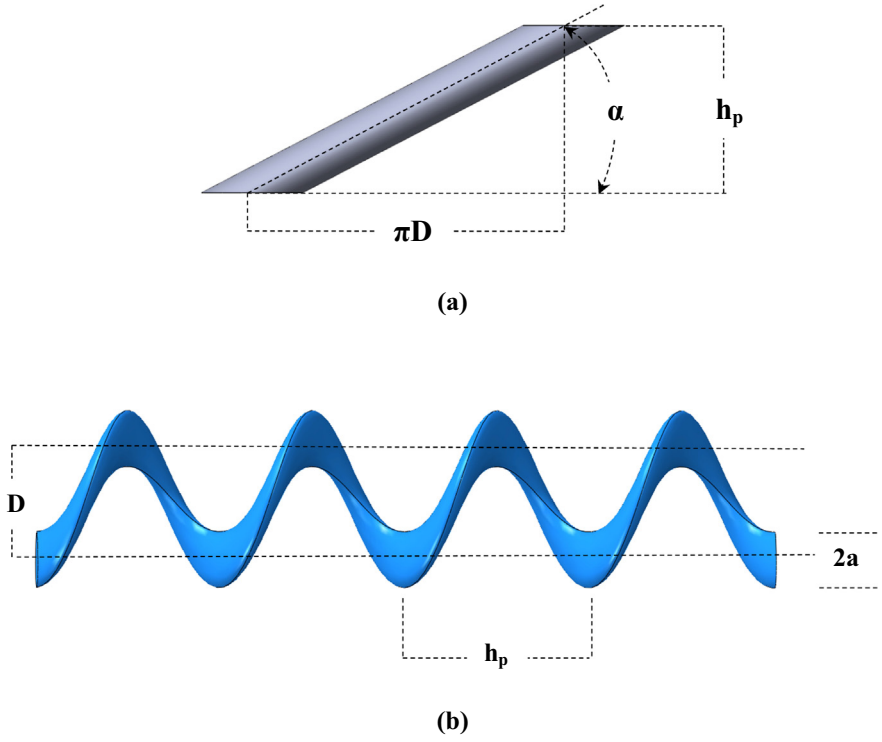

Fig. 4. (a) Definition of the pitch angle. The pitch angle is calculated by uncoiling one turn of a helix with πD circumference and pitch height h_p. (b) Geometrical spring parameters. The particular spring geometry corresponds to a 4-turn spring with 900 nm seed spacing.

(1). Moreover, the GLAD parameters, such as the seed spacing and the angular rotation speed of the substrate, simultaneously affect the coil diameter and the overlap between springs, or the coil diameter and the wire diameter. As a result, for the same number of coil turns per unit length, which is controlled by the substrate rotation speed, an increase in the seed spacing from 900 nm to 1500 nm reduced the overlap

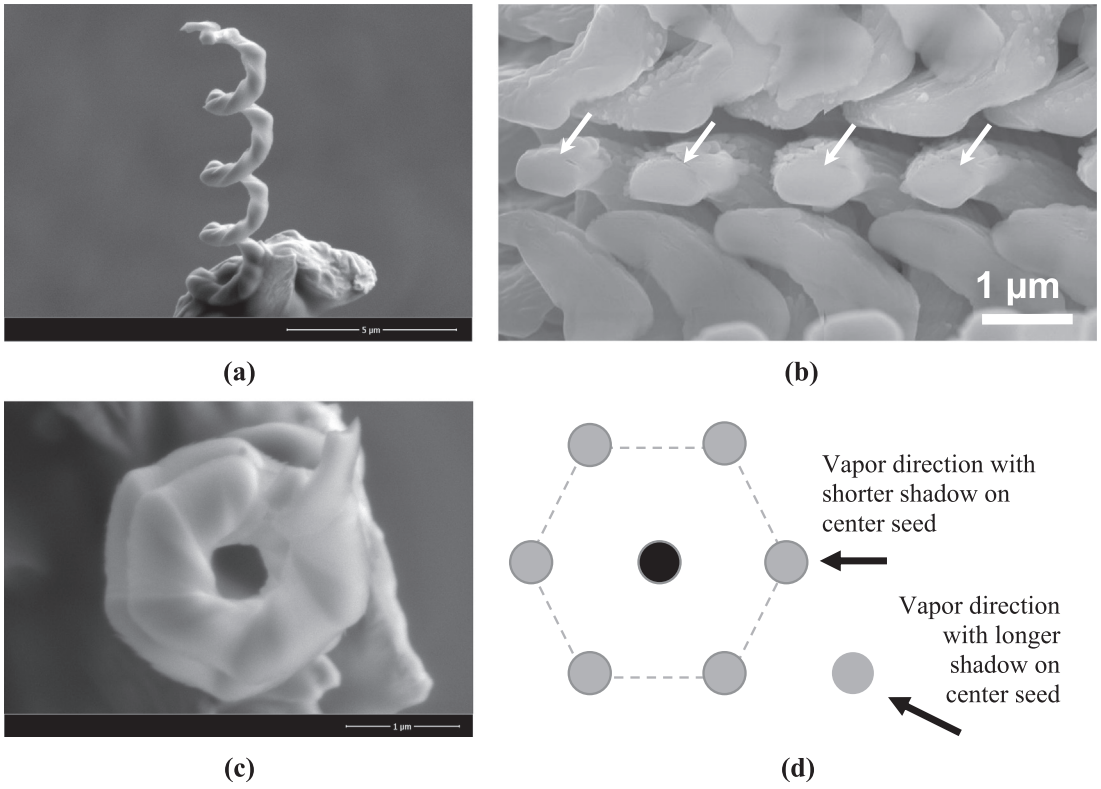

Fig. 5. (a) Side view of a 4-turn Si spring from a film with 900 nm seed spacing. (b) Section of a film of nanosprings by FIB-tomography at the growth angle of 32°, showing the elliptical cross-section of individual wires (pointed by the arrows) comprising the nanosprings. (c) Top view of the Si spring in (a). (d) Seeds arranged in a hexagonal pattern creating the shadowing conditions that lead to the hexagonal spring cross-section shown in (c).

Table 1
Geometrical parameters of Si nanosprings. The values in the table are the mean ± one standard deviation.

Spring type (number of turns, seed spacing)	Coil diameter (nm)	Major axis of coil wire (nm)	Minor axis of coil wire (nm)	Pitch (nm)
4 turns, 900 nm	1530 ± 40	380 ± 10	160 ± 10	2500
4 turns, 1500 nm	1570 ± 40	470 ± 25	250 ± 30	2500
10 turns, 900 nm	1060 ± 25	350 ± 20	200 ± 15	1000
10 turns, 1500 nm	1320 ± 25	N/A	N/A	1000

between springs but increased the wire dimensions, Table 1. Furthermore, during substrate rotation, shadowing of the incident vapor by adjacent springs causes the major axis of the elliptical wire cross-section to point towards the coil axis. Based on the aforementioned considerations, the geometrical parameters (major and minor axes) of the wires comprising each type of seeded Si nanospring were measured via SEM and FIB-tomography and are listed in Table 1. The minor and the major axes of the 10-turn springs in films with 1500 nm seed spacing are not reported because these structures deviated significantly from a coil-like geometry.

3.2. Material behavior of GLAD Si columns

The material behavior of Si fabricated by the GLAD process is not known, although the low temperature deposition implies that the structure is amorphous. Individual Si columns grown by GLAD were subjected to microscale tension to obtain the material elastic modulus and strength. Fig. 6 shows a force vs. extension graph of a Si column. The Si columns were slightly tapered along their length, which was taken into account in the calculation of the elastic modulus as:

$$E = \frac{kL}{\pi R_2 R_1} \tag{7}$$

where k is the specimen stiffness in [N/m], L is the gauge length and R_1 and R_2 are the radii at the two ends of the column. The average elastic modulus was calculated as 5.3 ± 1 GPa, which is ~5% of the elastic modulus (94 GPa) of aSi [24]. Using the smallest cross-sectional area as the likely location of failure, the strength of the Si columns was estimated as 97 ± 22 MPa, compared to the tensile strength of 425 ± 75 MPa of aSi films [24].

In order to shed light into the reasons for the low elastic modulus of the aSi columns compared to bulk aSi films, TEM imaging of individual aSi columns and springs was carried out to evaluate their microstructure. As shown in Fig. 7(a-c), the Si columns had a dendritic structure while the nanosprings were fibrillar comprised of bundled fine nanowires. Thus, in GLAD, substrate seeding "bundles" a large number of fine fibrils nucleating on each seed, and guides their growth in a tightly wound (springs) or dendritic (columns) superstructure. This microstructure resulted in lower density and, thus, material modulus, without, however, compromising the material strength. Due to their dendritic structure, GLAD columns support load mainly through their core, and the "branches" that are seen in Fig. 7(a), although comprise large part of the column's cross-section, actually carry a limited load. In comparison, the nanofibrils seen in the nanosprings in Fig. 7(b,c) are largely continuous and more closely packed in the case of 10-turn coils (Fig. 7(c)) compared to 4-turn coils in Fig. 7(b), as also deduced from the different density contrast in the TEM images. These differences are expected to result in different "material" properties for nanosprings with different geometry, and higher effective material modulus for nanosprings compared to columns. A comparison between the experimental spring stiffness and the calculated values from the FE models was employed in the next Sections to calculate the effective material modulus of the different types of GLAD nanosprings.

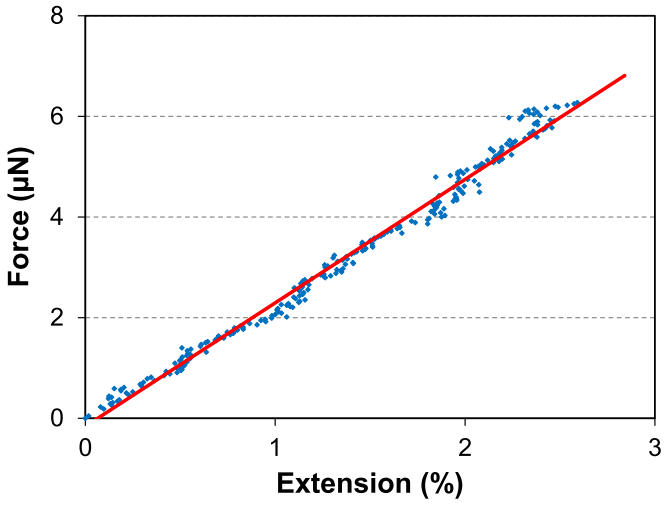

Fig. 6. Force vs. extension of an individual Si column, showing linearity up to 2.5% extension.

3.3. Tension/compression and bending behavior of individual Si nanosprings

The force vs. extension/compression curves provided the initial spring stiffness. The reliability of these measurements depends on the integrity of the FIB-deposited Pt tabs, which was confirmed after testing to ensure that failure was not initiated at the grips. All springs tested in tension or compression failed at random locations in the gauge section, as shown in Fig. 8(a–c). Fig. 8(d,e) show the force vs. spring extension and compression for the four types of seeded springs. Under tension, all springs behaved quite linearly, with a maximum extension of 8.4 ± 1.2% and 6.7 ± 1.0% for 4-turn springs with 900 nm and 1500 nm seed spacing, respectively, and 5.3 ± 1.5% and 2.2 ± 0.5% for 10-turn springs with 900 nm and 1500 nm seed spacing, respectively. Most spring types allowed for larger amounts of compression because of lateral deflection that was due to the eccentric loading of the springs, as deduced from the spring geometry shown in Fig. 4(b). The average compressive strain at failure was 17.4 ± 4.9% and 11.8 ± 2.0% for 4-turn springs with 900 nm and 1500 nm seed spacing, respectively, and 4.8 ± 1.3% and 3.5 ± 0.9% for 10-turn springs with 900 nm and 1500 nm seed spacing, respectively. The tensile stiffness was 7.7 ± 1.8 N/m and 18.5 ± 3.7 N/m for springs from films comprised of 4-turn coils with 900 nm and 1500 nm seeding, and 19.2 ± 1.2 N/m and 215 ± 88 N/m for springs from films comprised of 10-turn coils with 900 nm and 1500 nm seeding, respectively. Very similar were the initial compressive stiffness values which are reported in Table 2.

Bending tests with individual nanosprings, simulating film shear with constrained normal displacements, provided the bending stiffness as the slope of the bending force vs. deflection curves that were relatively linear until failure (Fig. 9(a)). The average bending stiffness ranged from 1.1 ± 0.4 N/m for 4-turn coils (900 nm seed spacing) to 31 ± 15 N/m for 10-turn coils (1500 nm seed spacing), as shown in Fig. 9(b). Notably, springs with 4 turns and 1500 nm seed spacing, and 10 turns with 900 nm seed spacing had virtually the same experimental tensile (18.5 ± 3.7 N/m vs. 19.2 ± 1.2 N/m) and bending stiffness (3.1 ± 1.4 N/m vs. 3.4 ± 1.3 N/m), yet the two types of springs produced films with very different intertwining (Fig. 1(d,e)). The ratio of the normal-to-bending stiffness of all types of springs was between 5.6 and 7.1, which is the same as the ratio of the effective Young's modulus-to-shear modulus of the nanospring films. This value is 2–4.5 times the ratio of Young's modulus to shear modulus of bulk metals (2.6), thus highlighting the versatility of nanospring films to attain combinations of elastic properties that are not possible in monolithic materials.

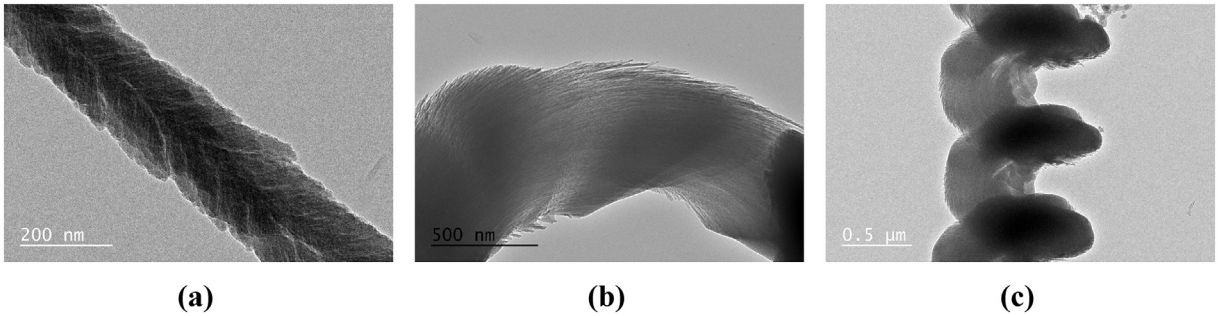

Fig. 7. TEM views of (a) a Si column, and Si springs comprised of (b) 4-turn and (c) 10-turn coils.

3.4. Analytical and numerical calculation of individual nanospring response

The analytical expressions in Eqs. (2) and (6) are approximate solutions for specific boundary conditions and large coil-to-wire diameter ratios as explained in [15,16,22,23]. Importantly, the analytical models calculate the stiffness of ideal coils constructed by "winding" a wire around a cylinder following a helical path. Due to shadowing, the major axis of the elliptical wire comprising the actual GLAD springs always points to the axis of symmetry of the spring. This consideration about the coil growth during GLAD, along with the measured dimensions reported in Table 1, were used in a FE analysis to compute the compressive and tensile stiffness of the individual springs in Fig. 1(c–e). The FE model geometry was generated starting with an ellipse with its major axis tilted by the growth angle of the springs (Fig. 10). The growth angle, measured from SEM images, was 32° for springs with 4-turns, and 42° for springs with 10 turns. An example of the meshed model of a 4-turn spring, from a film with 900 nm seed spacing, is shown in Fig. 10. The FE calculations were conducted in ABAQUS™ using quadratic tetrahedral elements (C3D10) and a fine mesh. All six degrees of freedom were fixed at one spring end, and the other end was displaced along the coil axis while constraining all other degrees of freedom. These FE models approximated the tension/compression tests with individual nanosprings using MEMS. The FE models were first benchmarked against the analytical solutions in Eqs. (1) and (5) for ideal coils with circular wire geometry and the same coil-to-wire diameter ratios as in the present springs. For 4-turn springs, the analytical predictions by Eqs. (1) and (5) were in excellent agreement with the FE results, thereby providing confidence in the FE model parameters. Eqs. (1) and (5) overpredicted the tensile stiffness of the 10-turn springs with 900 nm seed spacing by 11.5% and 15.2%, respectively, due to the reduction in the coil-to-wire diameter ratio from ~3 for 4-turn springs to ~2 for 10-turn springs. This is because both Eqs. (1) and (5) are more accurate for larger coil-to-wire diameter ratios.

Next, a FE analysis was carried out for the true geometry of all types of seeded nanosprings in Fig. 1, except for the 10-turn springs with 1500 nm seed spacing which were not spring-like. Analytical and FE calculations using the elastic modulus of the Si columns (5.3 ± 1 GPa) resulted in nanospring stiffness values that were an order of magnitude

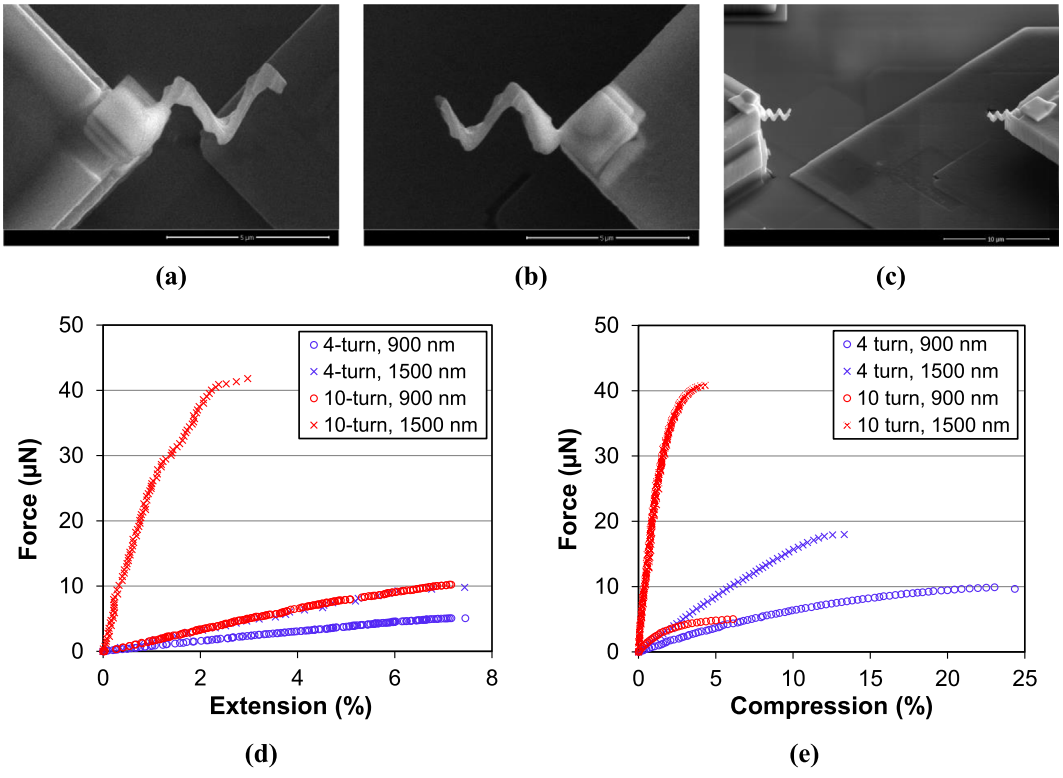

Fig. 8. Matching failure segments of a (a,b) 4-turn and (c) 10-turn Si spring, from films with 900 nm seed spacing, after subjected to tension. Force vs. (d) extension, and (e) compression of individual 10-µm long Si springs.

Table 2
Normal stiffness of 10-μm long nanosprings derived from experiments. The standard deviation values were computed from the results of at least three tests.

Spring type (# turns, seed spacing)	Compressive stiffness (N/m)	Tensile stiffness (N/m)
4 turns, 900 nm	7.3 ± 2.1	7.7 ± 1.8
4 turns, 1500 nm	17.0 ± 1.5	18.5 ± 3.7
10 turns, 900 nm	23.0 ± 1.4	19.2 ± 1.2
10 turns, 1500 nm	187 ± 19	215 ± 88

smaller than the experimental values. This result, corroborated by the TEM images of the different microstructure of the GLAD columns and springs, provided a strong indication that the material properties of the different nanostructures fabricated by GLAD depend on the packing and continuity of the fine nanofibrils. Therefore, the effective elastic modulus was extracted for different nanospring types by comparison of the FE calculations with the experimental data from tension tests. The monotonic relationship between the spring constant and the shear modulus, Eq. (5), simplifies the solution of the inverse problem and minimizes the error in the calculation of the shear modulus. In the absence of further quantitative information, the Young's modulus was calculated from the shear modulus by assuming isotropy and a Poisson's ratio value of 0.22 [25]. For 4-turn nanosprings with either 900 nm or 1500 nm seed spacing, a Young's modulus value of 40 GPa provided an agreement between the experimental and the FE tension/compression values of the nanospring stiffness (Fig. 11). Similarly, for the 10-turn nanosprings, a Young's modulus of 53 GPa provided an agreement between the experimental tensile stiffness and the FE calculations (Fig. 11). Given the nanofibrillar structure of the Si nanosprings, the true Poisson's ratio can be very different from the value of bulk aSi. However, the spring stiffness is a weak function of the Poisson's ratio: a 10% uncertainty in the value of the Poisson's ratio results in 1.6% uncertainty in the calculated spring stiffness.

The calculated Young's moduli for 4- and 10- turn nanosprings were also used in the modified analytical solutions given by Eqs. (2) and (6). In Eq. (2) the moment of inertia I was substituted by $I_a = \pi ab^3/4$ for an

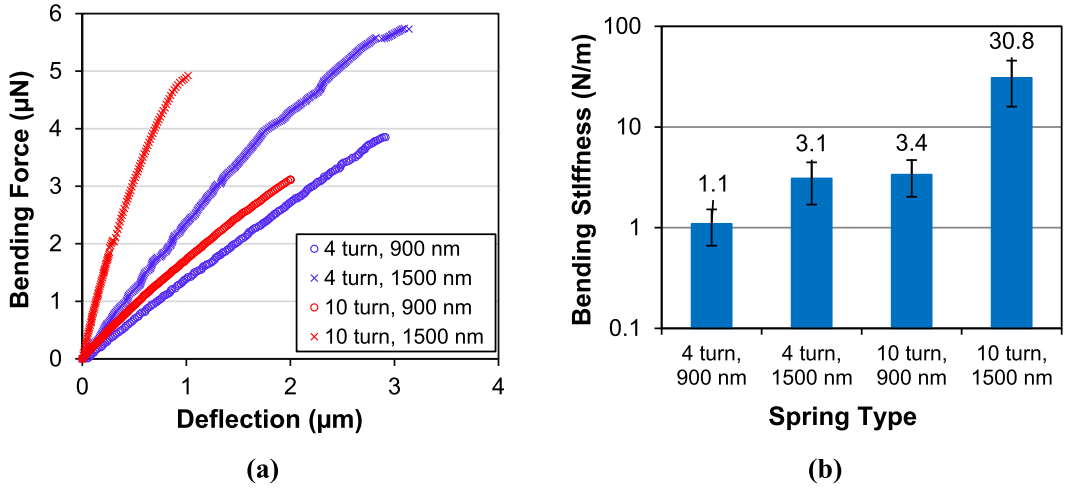

Fig. 9. (a) Bending force vs. deflection of 10-μm long Si nanosprings. (b) Spring bending stiffness. Logarithmic scale is used to show all results in the same graph.

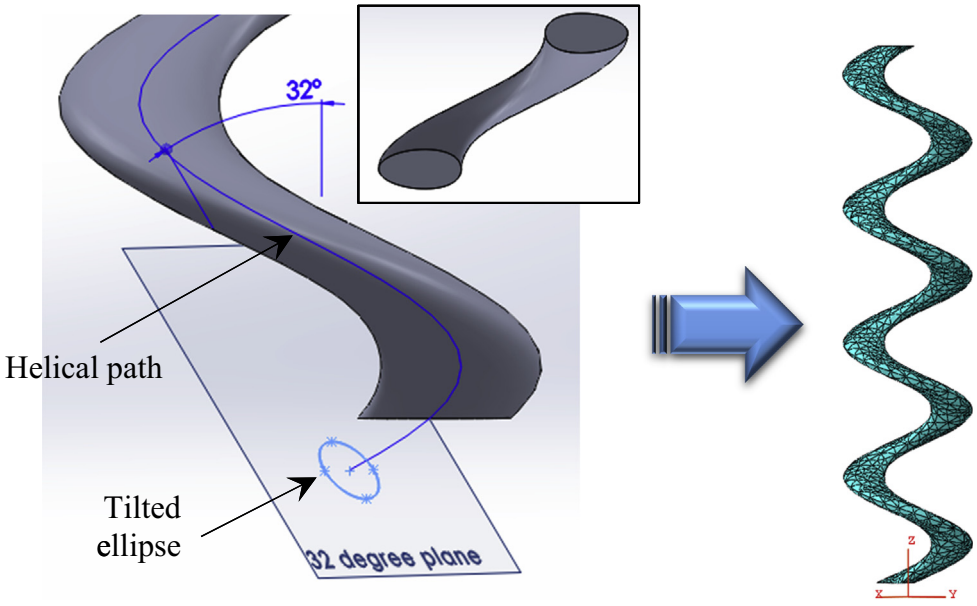

Fig. 10. (Left) Si spring model generated with a 32° tilted elliptical wire cross-section. Inset shows the elliptical cross-section of the coil wire. (Right) Meshed view of a 4-turn spring constructed based on the geometry shown on the left.

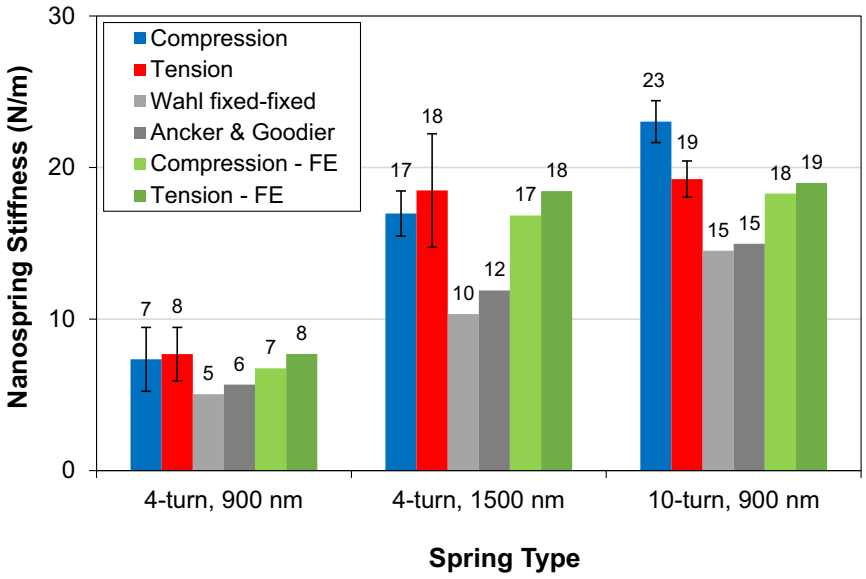

Fig. 11. Stiffness of 10-μm long Si nanosprings, as derived from experiments, analytical and FE models. The stiffness values at the top of each bar have been rounded to the closest integer.

elliptical cross-section. As shown in Fig. 11, both analytical models consistently underpredicted the experimental spring stiffness by 20–40%. The difference in values between the analytical models and the experiments must be put in perspective of the uncertainty in the estimated spring stiffness. For example, small errors in the major and minor wire axes, as well as variations of these values along a spring,

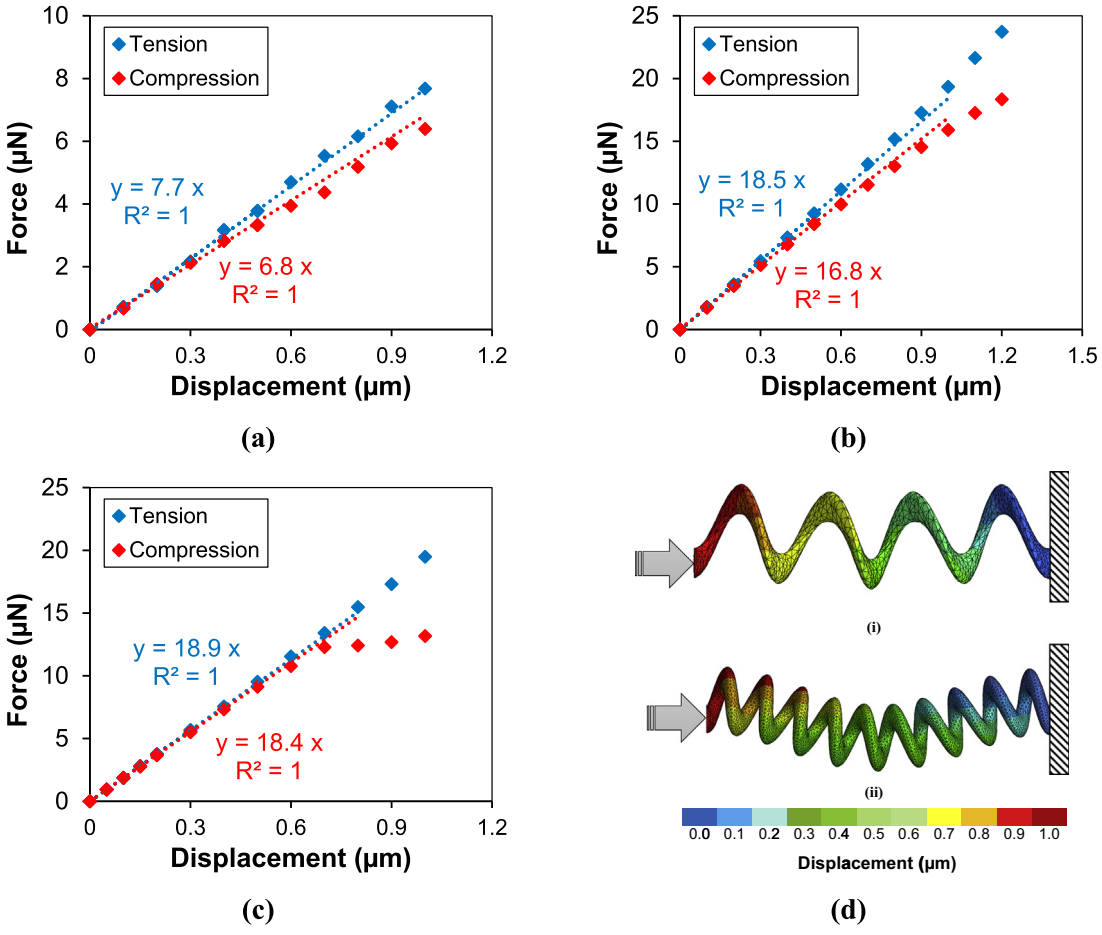

Fig. 12. Force vs. end displacement of a 4-turn spring with (a) 900 nm and (b) 1500 nm seed spacing, and a (c) 10-turn spring with 900 nm seed spacing, subjected to tension (blue) and compression (red). All curves are for 10-μm long springs. (d) Deformed geometry of a (i) 4-turn spring and a (ii) 10-turn spring, both from films with 900 nm seed spacing, subjected to 10% compression, showing the buckling profile of the 10-turn spring. Both spring ends are constrained for rotation and lateral deflection. (For interpretation of the references to colour in this figure legend, the reader is referred to the web version of this article.)

are amplified when calculating the spring stiffness: a 10% overestimate in the value of the minor axis of a 4-turn spring (900 nm seed spacing) would result in 29% increase in the stiffness predicted by Eqs. (2) and (6). Thus, the lower values predicted by the analytical models are within the uncertainly in determining the geometry and material properties of GLAD nanosprings.

Furthermore, the FE model provided insights into the deformation mode of each type of nanospring. Both types of 4-turn springs deformed uniformly both in tension and in compression with small deviations between the tensile and the compressive response (Fig. 12(a,b)). On the contrary, the smaller coil-to-wire radius ratio of 10-turn coils resulted in spring buckling after 7.5% compression (Fig. 12(c,d)). A similar response was observed in in situ SEM compression experiments of films comprised of the same type of nanosprings [26]. The term *buckling* is not used in its strict sense in this case, because no sudden instability took place, rather a continuous lateral spring deflection until sudden failure. In both cases of 4-turn springs, the initial compressive stiffness agreed well with the tensile stiffness, but its value declined with increasing force because the FE model simulated the true GLAD springs which were loaded off-axis because the spring ends do not lie along the spring axis (Fig. 4(b)), thus resulting in increasing lateral spring deflection under compression.

Finally, a comment is due about the implications of individual nanospring properties on the effective response of their films. Given the seed spacing and the range of the individual tensile and bending spring stiffness values (7–215 N/m and 1–31 N/m), the normal and shear stiffness of films comprised of these four types of springs are estimated to be in the range 90–1000 MPa and 15–150 MPa, respectively, namely well in the range of elastomers and thermoplastics. For the most compliant 4-turn spring films, the ultimate tensile strain was up to 8% and the shear strain as high as 30%, which further underscore the robustness of thin films fabricated of brittle materials in the form of compliant nanosprings.

4. Conclusions

The mechanical behavior of individual building blocks in thick films comprised of aSi nanosprings was obtained for different geometrical parameters and types of loading. TEM characterization and FIB-tomography provided new insights into the microstructure of GLAD materials: The seeding process was shown to bundle a very large number of fine fibrils nucleating on each seed and guide their growth in a tightly wound (springs) or dendritic (columns) superstructure. This microstructure resulted in lower density and, thus, material modulus compared to bulk aSi films deposited at low temperatures. Si columns were shown to have the lowest elastic modulus of 5.3 GPa, while the effective Young's moduli of the material comprising the 4-turn and 10-turn nanosprings were estimated to be 40 GPa and 53 GPa, respectively. Nanosprings with the same number of turns per unit height had the same material modulus. It was shown that the dimensions and seed spacing of GLAD nanosprings could be designed to obtain a broad range of very low normal (90–1000 MPa) and shear (15–150 MPa) film stiffness. The experimental and modeling results presented in this paper provide quantitative evidence of the versatility of nanosprings as building blocks in the design of highly compliant interphases and films with combinations of normal and shear stiffness values that are not possible in bulk materials.

Data availability

The raw/processed data required to reproduce these findings cannot be shared at this time as the data also form part of an ongoing study.

Funding

This work was supported by the Air Force Office of Scientific Research (AFOSR) [grant numbers FA9550-13-1-0149, FA9550-15-1-0470].

Acknowledgements

The authors acknowledge the support by the Air Force Office of Scientific Research (AFOSR) through grants FA9550-13-1-0149 and FA9550-15-1-0470 with Dr. B.L. Lee as the program manager. We also thank Prof. M. Brett from the University of Alberta for his input on the fabrication of the GLAD films, and Ms. Ching-Yen Tang from the University of Illinois for her assistance with TEM imaging.

References

[1] D.A. Antartis, R.N. Mott, D. Das, D. Shaddock, I. Chasiotis, Cu nanospring films for advanced nanothermal interfaces, Adv. Eng. Mater. (2018) 1700910, https://doi.org/10.1002/adem.201700910.
[2] B.D. Polat, O. Keles, K. Amine, Silicon-copper helical arrays for new generation lithium ion batteries, Nano Lett. 15 (2015) 6702–6708.
[3] B.D. Polat, O. Keles, K. Amine, Compositionally-graded silicon-copper helical arrays as anodes for lithium-ion batteries, J. Power Sources 304 (2016) 273–281.
[4] B.D. Polat, O. Keles, Designing self-standing silicon-copper composite helices as anodes for lithium ion batteries, J. Alloys Compd. 677 (2016) 228–236.
[5] M. Hawkeye, M.J. Brett, Glancing angle deposition fabrication, properties, and applications of micro- and nanostructured thin films, J. Vac. Sci. Technol. A 25 (2007) 1317–1335.
[6] M.T. Taschuk, M.M. Hawkeye, M.J. Brett, Glancing angle deposition, Handbook of Deposition Technologies for Films and Coatings, 3rd editionElsevier, Burlington, 2010.
[7] Y. Zhao, Growth and synthesis of nanostructured thin films, Integrated Analytical Systems 2009, pp. 31–64.
[8] A. Barranco, A. Borras, A.R. Gonzalez-Elipe, A. Palmero, Perspectives on oblique angle deposition of thin films: from fundamentals to devices, Prog. Mater. Sci. 76 (2016) 59–153.
[9] J. Lintymer, N. Martin, J.M. Chappé, P. Delobelle, J. Takadoum, Influence of zigzag microstructure on mechanical and electrical properties of chromium multilayered thin films, Surf. Coat. Technol. 180-181 (2004) 26–32.
[10] U. Allenstein, E.I. Wisotzki, C. Gräfe, J.H. Clement, Y. Liu, J. Schroers, S.G. Mayr, Binary Fe-Pb submicron structures fabricated through glancing angle deposition (GLAD) for bioapplications, Mater. Des. 131 (2017) 366–374.
[11] T. Sumigawa, S. Chen, T. Yukishita, T. Kitamura, In situ observation of tensile behavior in a single silicon nano-helix grown by glancing angle deposition, Thin Solid Films 636 (2017) 70–77.
[12] M. Malac, R.F. Egerton, M.J. Brett, B. Dick, Fabrication of submicrometer regular arrays of pillars and helices, J. Vac. Sci. Technol. B 17 (1999) 2671–2674.
[13] M.W. Seto, K. Robbie, D. Vick, M.J. Brett, L. Kuhn, Mechanical response of thin films with helical microstructures, J. Vac. Sci. Technol. B 17 (1999) 2172–2177.
[14] M.W. Seto, B. Dick, M.J. Brett, Microsprings and microcantilevers: studies of mechanical response, J. Micromech. Microeng. 11 (2001) 582–588.
[15] C.J. Ancker, J.N. Goodier, Pitch and curvature corrections for helical springs, J. Appl. Mech. (1958) 466–470.
[16] C.J. Ancker, J.N. Goodier, Theory of pitch and curvature corrections for the helical springs – I (tension), J. Appl. Mech. (1958) 471–483.
[17] H. Hirakata, S. Matsumoto, M. Takemura, M. Suzuki, T. Kitamura, Anisotropic deformation of thin films comprised of helical springs, Int. J. Solids Struct. 44 (2007) 4030–4038.
[18] T. Sumigawa, H. Hirakata, M. Takemura, S. Matsumoto, M. Suzuki, T. Kitamura, Disappearance of stress singularity at interface edge due to nanostructured thin film, Eng. Fract. Mech. 75 (2008) 3073–3083.
[19] D.L. Liu, D.X. Ye, F. Khan, F. Tang, B.K. Lim, R.C. Picu, G.C. Wang, T.M. Lu, Mechanics of patterned helical Si springs on a Si substrate, J. Nanosci. Nanotechnol. 3 (2006) 492–495.
[20] M. Naraghi, I. Chasiotis, H. Kahn, Y. Wen, Y.A. Dzenis, Novel method for mechanical characterization pf polymeric nanofibers, Rev. Sci. Instrum. 78 (2007) (085108-1-8).
[21] M. Naraghi, I. Chasiotis, Optimization of comb-driven devices for mechanical testing of polymeric nanofibers subjected to large deformations, J. Microelectromech. Syst. 18 (2009) 1032–1046.
[22] A.M. Wahl, Mechanical Springs, 1st edition Penton Publishing Company, Cleveland, 1944.
[23] A.M. Wahl, Mechanical Springs, 2nd edition McGraw-Hill, New York, 1963.
[24] D. Antartis, I. Chasiotis, Residual stress and mechanical property measurements in amorphous Si photovoltaic thin films, Sol. Energy 105 (2014) 694–704.
[25] L.B. Freund, S. Suresh, Thin Film Materials: Stress, Defect Formation and Surface Evolution, Cambridge University Press, Cambridge, 2003.
[26] D.A. Antartis, R.N. Mott, I. Chasiotis, Si nanospring films for compliant interfaces, J. Mater. Sci. 53 (2018) 5826–5844.